SACLANTCEN REPORT
serial no: SR-268

*SACLANT UNDERSEA RESEARCH CENTRE REPORT*

# A PARAMETRIC SYNTHETIC APERTURE SONAR FOR DETECTION OF PROUD AND BURIED MINES

*S. Fioravanti, A. Maguer, A. Løvik*

December 1997

**Report no. changed (Mar 2006): SR-268-UU**



SACLANT Undersea Research Centre
Viale San Bartolomeo 400
19138 San Bartolomeo (SP), Italy

tel: +39-187-540.111
fax: +39-187-524.600

e-mail: library@saclantc.nato.int

**NORTH ATLANTIC TREATY ORGANIZATION**

SACLANTCEN SR-268

# A Parametric Synthetic Aperture Sonar for Detection of Proud and Buried Mines

S. Fioravanti, A. Maguer, A. Løvik

---

The content of this document pertains to work performed under Project 031-1 of the SACLANTCEN Programme of Work. The document has been approved for release by The Director, SACLANTCEN.

Jan L. Spoelstra
Director

intentionally blank page

# A Parametric Synthetic Aperture Sonar for Detection of Proud and Buried Mines

S. Fioravanti, A. Maguer, A. Løvik

**Executive Summary:** The problem of detecting and classifying buried mines is of major importance to many NATO operations. Mines are usually detected by high-frequency (around 100 kHz) sonar systems, which are severely limited in effectively detecting buried targets due to strong absorption of high-frequency sound by the seabed top layer.

The Centre has investigated a number of alternative approaches including the use of parametric sonar used as a sidescan sonar designed to work at very low grazing angles (both above and well below the critical angles). The main advantage of parametric sonar is the low-frequency wave with high-directivity (c.f. the primary frequency) and wide bandwidth but without sidelobes, which penetrate more deeply into the sediment. The major advantage of the low grazing angle option in shallow water is the potential to cover large areas compared to the traditional systems using normal incidence or swath survey approaches. However, this low grazing angle option is very challenging, as it is commonly accepted in underwater acoustics that limited penetration into the sediment will occur below a given critical angle. There is nonetheless substantial evidence of penetration below the critical grazing angle, which supports the viability of this approach.

In this report, it is experimentally demonstrated that the detection of buried objects is possible using a sonar operating at grazing angles below the critical angle, the small loss in dB demonstrating that the sound was penetrating well into the sediment. It was also demonstrated that, for the bottom type considered, low-frequency sonar was superior (in terms of proud target detection performance) to high-frequency sonar. Further theoretical studies and experiments will be performed to understand the underlying physical theory of sub-critical angle penetration into the sediment and to estimate the performance of the TOPAS sonar for the detection of buried objects.

Synthetic Aperture Processing was shown to significantly improve the parametric sonar detection performance and also provided accurate location of all targets. More experiments will be performed to estimate the sensitivity of synthetic aperture processing to the motion of the tow-body. It is also intended to start work on auto-focusing techniques that could be applied to synthetic aperture processing in order to accurately estimate the platform motion.

intentionally blank page

**A Parametric Synthetic Aperture Sonar for Detection of Proud and Buried Mines**

S. Fioravanti, A. Maguer, A. Løvik

**Abstract:** This paper describes an experimental comparison between a parametric sonar and a conventional sonar for the detection of small objects on and in, the sea bed. Two experiments were performed in France (GESMA site) in October 95 and March 96 in order to assess the feasibility of detecting buried mines using a parametric sonar configured as a sidescan sonar working at very low grazing angles (well below the critical angle) where the Snell theory restricts any bottom type 2 penetration of the sound into the sediment. There is however substantial evidence of penetration below the critical grazing angle which may be explained by different theories (such as for example bottom roughness, evanescent waves, Biot waves, Narrow beam-width).

In the two experiments the parametric array was mounted on a platform which was able to move linearly at a constant speed (0.25 m/s) on a rail. Objects were positioned on and in the sea bed at ranges from 17 m to 60 m. The buried targets were detected at grazing angles of the order of 16°, well below the critical angle of 28°. The comparison of the Peak Signal to Bottom Reverberation Ratio (PSSR) obtained with high and low-frequency is performed for the proud and buried targets. It is shown that the PSSR is of the order of 5 dB higher for the low-frequency than for the high-frequency due mainly to the higher level of bottom reverberation at high-frequency. It is shown that detection of buried targets was only possible with low frequencies, emphasizing that sub-critical penetration into the sediment is possible. No detection was observed with the high-frequency due to the higher attenuation into the sediment at this frequency. While the sonar was moving on the rail it was possible to perform synthetic aperture sonar processing with the parametric array. Significant improvements in resolution and signal-to-noise ratio were also obtained by integrating successive pings transmitted while the sonar was in motion. The proud targets were precisely located within the mine field and gains of 10 dB and 5 dB respectively were obtained for the proud and buried targets.

**Keywords:** Parametric sonar, Synthetic Aperture Sonar, Detection of buried objects

intentionally blank page

# Contents

intentionally blank page

# 1 Introduction

The problem of detecting and classifying buried mines is one of the more important identified short-falls in NATO. Mines are usually detected by high-frequency (around 100 kHz) sonar systems which due to strong absorption of high-frequency sound by bottom sediment, are severely limited in effectively detecting buried targets.

The Centre has investigated a number of alternative approaches including the use of parametric sonar [1] mounted as sidescan sonar designed to work at very low grazing angles (well beyond the critical angles). The main advantage of a parametric sonar is the low-frequency, high-directivity wave of primary frequency and wide bandwidth which penetrates deeply into the sediment. The main limitation of parametric sonar is poor efficiency at low frequency. The sonar selected by the Centre is the SIMRAD TOPAS sonar with a primary frequency around 40 kHz and a secondary frequency of 2 to 12 kHz.

A major advantage of the low grazing angle option, in shallow water, is the potential to cover large areas compared to the traditional systems using normal incidence or swath survey approaches. This low grazing angle option is very challenging however, given that according to classical reflection theory there is no penetration into the sediment. Thus no detection of buried objects should be possible while working below the critical angle. There is however substantial evidence of penetration below the critical grazing angle, which justifies the selected approach. At present, four mechanisms have been hypothesized. For example the porous nature of the sediment leads to a second "slow" compressional wave with a wave speed less than the speed of sound in the water [2], the roughness of the water-sediment interface [3], the effect of using a narrow beamwidth [4] and the volume inhomogeneities within the sediment which scatter the evanescent wave [5].

The objective of this work is to demonstrate the feasibility of the detection of buried targets while working at sub-critical grazing angle incidence. The spatial resolution obtained with the system synthetic aperture processing, generated very fine resolution irrespective of detection range. The ideal synthetic aperture is perfectly linear and reduces to a straightforward extension of a conventional beamformer applied to successive pings. However, the motion of the platform distorts the synthetic aperture which has to be compensated for by either using an inertial navigation system on the tow-body which will allow a very accurate control of the platform motion or auto-focusing techniques that will adaptively correct the distorted array. Numerous auto-focusing techniques have been described in the literature [6,7,8]. In this study, as all the data have been collected with the sonar moving on a rail and therefore with no motion effect, none of the auto-focusing techniques developed in the literature has been considered. Moreover, the parametric

sonar, coupled with synthetic aperture processing, having longer wavelength, wide bandwidth and also a beam pattern with no side-lobes should be less sensitive to array motion [9].

In order to assess the feasibility of detecting buried mines while working below critical angles but also the detection of proud mines, with the TOPAS parametric sonar, two experiments were carried out in Brest at the Gesma rail site in October 95 and March 96. The parametric sonar was mounted on a 12 m rail on which the sonar moved at a constant speed (0.25 m/s). Data were collected at fixed positions and while the sonar was in motion. Ricker pulses and Chirp signals were used and recorded.

# 2

# Synthetic Aperture Processing

## 2.1 Hypothesis and Modeling

The aim of synthetic aperture processing is to increase azimuthal resolution by using a focused virtual array.

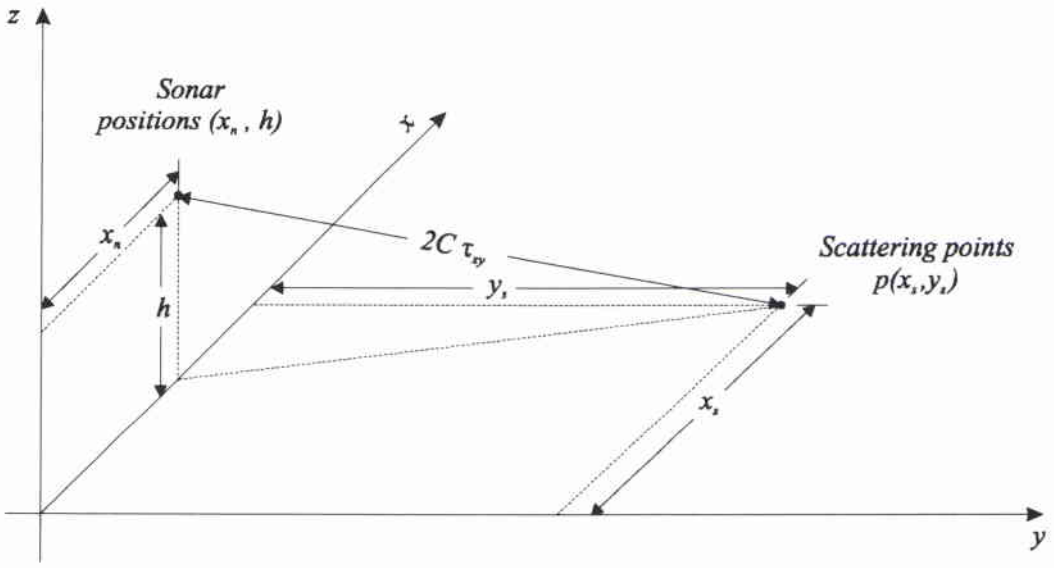


*Figure 1: The geometry*

In the following equation a simple acoustic model is considered. The scene is considered as a set of scatter points $P(x_s,y_s)$ with a frequency independent impulse response

$$A_{x,y}(\omega) = A_t(x_s,y_s) \tag{1}$$

where $A_t(x_s,y_s)$ is the backscattering strength of the point target where in the following the index $s$ will be omitted for clairty. Therefore, given a transmitted signal $s(t)$, a platform speed $v$, a ping repetition frequency $PRF$, a sonar height $h$ from the sea bottom and therefore a sonar position

$$x_n = n \cdot \Delta x \text{ where } \Delta x = v \times \frac{1}{PRF} \tag{2}$$

the received backscattering $e^{xy}(t)$ from a point target at a position $P(x,y)$ is given by the equation

$$e_n^{xy}(t) = B\big(\theta(x_n, x, y)\big) A_t(x, y) s\big(t - \tau_{x,y}\big) \tag{3}$$

where the delay $\tau_{x,y}$ is given by:

$$\tau_{x,y} = \frac{1}{2C}\sqrt{y^2 + (x_n - x)^2 + h^2} \tag{4}$$

The $B(\theta)$ term represents the sonar beam pattern. The angle $\theta$ is the angle between the normal vector $\vec{D}$ to the sonar plane and the vector $\vec{P}_n(x,y) = \{(x_n - x), y, h\}$ that connects the sonar (position $P(x_n,0)$) to the point $P(x,y)$.

$$\theta(x_n, x, y) = \arccos\left(\frac{\vec{D} \cdot \vec{P}(x,y)}{\|\vec{D}\| \cdot \|\vec{P}(x,y)\|}\right) \tag{5}$$

The resulting signal received at the sonar position $n$ is the linear superimposition of the contribution of all the scattering points

$$e_n(t) = \sum_{xy} B\big(\theta(x_n, x, y)\big) A(x, y) s\big(t - \tau_n(x, y)\big) \tag{6}$$

Therefore, in the Fourier space, the contribution from each point $P(x,y)$ and the overall received signal are respectively

$$E_n^{xy}(\omega) = B\big(\theta(x_n, x, y)\big) A_t(x, y) S(\omega) e^{-j\omega\tau_{x,y}} \tag{7}$$

and

$$E_n(\omega) = S(\omega) \sum_{x,y} B\big(\theta(x_n, x, y)\big) A_t(x, y) e^{-j\omega\tau_{x,y}} \tag{8}$$

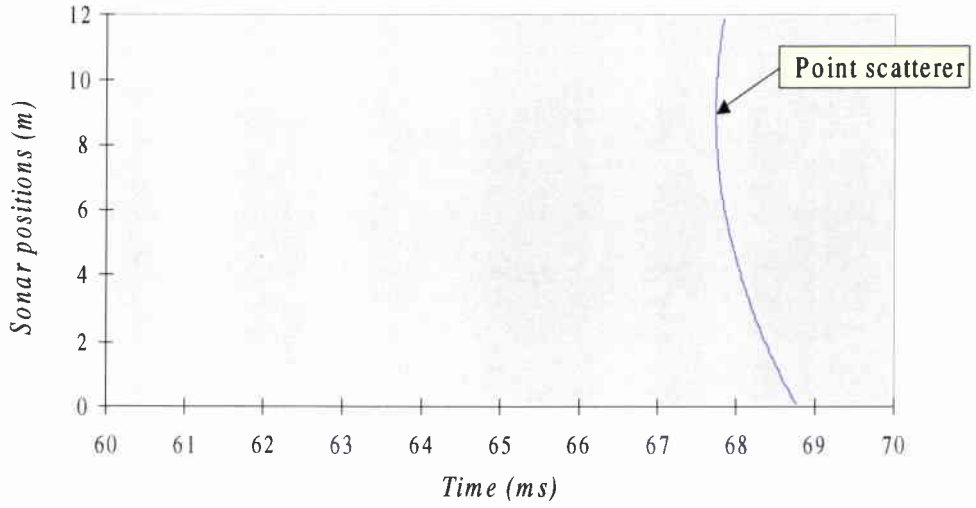


*Figure 2: Trajectory of a point target*

Under realistic conditions a noise term $N(\omega)$ must be added to the received signal

$$\frac{E_n(\omega)+N(\omega)}{S(\omega)} = C(\omega) = \sum_{x,y} B(\theta(x_n,x,y))A_t(x,y)e^{-j\omega\tau_{x,y}} + N(\omega) \tag{9}$$

Eqn. (9) combines the maximum obtainable joint resolution $(x,y)$ with the bandwidth of the input signal $S(\omega)$, the noise $N(\omega)$, and the beam pattern $B(\theta)$.

In fact, a theoretical solution can be computed by inverting the relation identified by the aforementioned equation. The result is a system of $L$ equations (where $L$ is given by the product $N\times\Omega$ with $\Omega$ being the number of frequencies $\omega_i$ with $S(\omega_i) \neq 0$, and $N$ being the selected number of pings in the synthetic antenna), and $M$ variables (given by the number of points $(x_i,y_j)$).

A stable least square solution can be achieved if $N >> M$.

### *2.2 The Doppler effect*

When dealing with moving objects the Doppler effect has to be taken into account. In this case the relative movement is due to the sonar speed. When looking at an angle $\theta=90°$ with respect to the movement vector, the relative speed of two points $P_1$ and $P_2$ (Figure 3) is different.

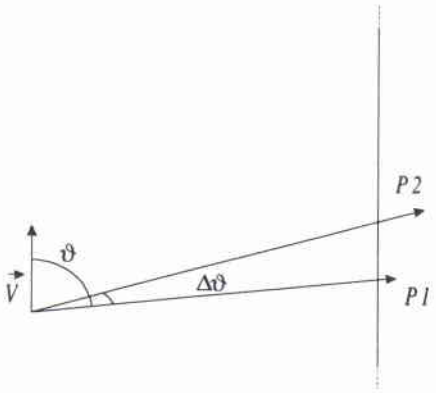


*Figure 3: The Doppler effect*

The generic Doppler frequency shift $f_D$ for a point P at an angle θ between the displacement vector $\vec{P}$ and the sonar motion vector $\vec{V}$ is given by:

$$f_D(P) \cong \frac{2v}{\lambda}\cos(\theta) \tag{10}$$

where $v = \|\vec{V}\|$ is the speed of the sonar, and λ is the wavelength of the transmitted signal. For the two generic points $P_1$ and $P_2$ the situation is:

$$f_D(P_1) \cong \frac{2v}{\lambda}\cos(\theta) \tag{11}$$

$$f_D(P_2) \cong \frac{2v}{\lambda}\cos(\theta + \Delta\theta) \tag{12}$$

and therefore

$$\Delta f_D(P_1, P_2) \cong \frac{2v}{\lambda}\Delta\theta\sin(\theta) \tag{13}$$

By substituting the adopted values of velocity (in this case 0.25 m/s), wavelength (around 0.25 m), and the angle (the worst case is 90°), it may be verified that the frequency shift is negligible.

### *2.3 Image Reconstruction Methods*

The approach adopted to reconstruct the image $A_I(x,y)$ making use of seismic coherent stacking is given by:

$$\tilde{A}_t(x_i, y_i) = \sum_n \tilde{B}\left(\theta(x_n, x_i, y_j)\right)\hat{e}_n(t_n) \tag{14}$$

where

$$t_n = \frac{1}{2C}\sqrt{y_j^2 + (x_n - x_i)^2 + h^2} \tag{15}$$

and $\hat{e}_n(t)$ is the complex quadrature signal.

The term $\hat{B}(\theta)$ takes into account the beam pattern $B(\theta)$ effects.

$$\hat{B}(\theta) = \begin{cases} 1.0 & \text{if } B(\theta) > THR \\ 0.0 & \text{if } B(\theta) < THR \end{cases} \tag{16}$$

The threshold *THR* is set according to the measured signal to reverberation ratio.

In a simple case where the beam pattern is constant (i.e., $B(\theta)=1$), and the transmitted signal has infinite bandwidth (i.e., $s(t) = \delta(t)$), $\tilde{A}_t(x_i, y_j)$ is easily deduced from Eq. (14) and is given by:

$$\begin{aligned} \tilde{A}_t(x_i, y_j) &= \sum_n e_n\left(\tau_n(x_i, y_j)\right) = \\ &= \sum_n \sum_{x_k, y_l} A(x_k, y_l) e_n\left(\tau_n(x_i, y_j) - \tau_n(x_k, y_l)\right) = \\ &= N \cdot A(x_i, y_j) + R_n(x_i, y_j) \end{aligned} \tag{17}$$

The result is that the amplitude of the scattering at the point $P(x,y)$ is amplified $N$ times, while in the case of noise (or reverberation) with zero mean, the term $R_n(x,y)$ is negligible.

It can be observed that $\tilde{A}_t(x, y)$ is given by the sum of the amplitude of the scattering point $P(x, y)$ amplified $N$ times and of a term $R_n(x, y)$ which is a sum of all the noise and reverberation contributions obtained over the $N$ considered points. In case of noise (or reverberation) with zero mean distribution, the latter term $R_n(x, y)$ tends to zero and is therefore negligible.

intentionally blank page

# 3 Experimental configuration

## 3.1 Overview

Two experiments were carried out in a precisely controlled environment at the Gesma testing facilities in Brest during October 1995 and March 1996. The goal of the first experiment was to assess the performance of a synthetic aperture approach combined with parametric sonar. The objectives of the second test were to evaluate the possibility of detecting buried objects with a very low grazing angle using a parametric sonar and also, if successful, to evaluate the gain obtained with the SAS on these data.

## 3.2 The Rail

The rail is mounted on a concrete base in the sea. A trolley can travel in both directions at a uniform speed $v$ of 0.10 m/s or 0.25 m/s. Vertical adjustments may be made to facilitate installation of equipment and to compensate for tidal fluctuations.

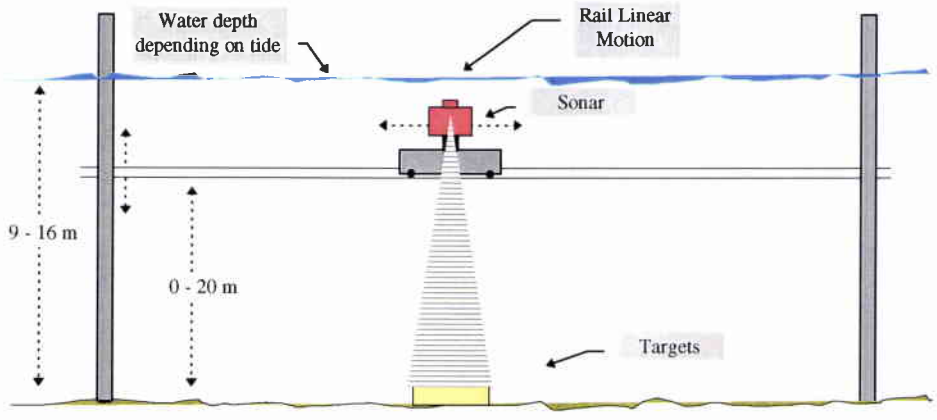


*Figure 4: Rail front view*

The sonar transducer was mounted on the rail platform at a tilt angle of 15°. The sonar tilt angle may be altered by electronic beam steering..

| *Rail characteristics* | |
|---|---|
| *length* | 13.5 *m* |
| *vertical range* | 0÷20 *m* |
| *water depth* | 9÷16 *m* (depending on the tide) |
| *platform speed* | 0.25*m/s* or 0.1 *m/s* |
| *bottom type* | gravel / coarse sand |

*Table 1: Rail characteristics*

Figure 5 shows the recorded ambient noise power spectrum generated by the platform measured in dB/μ Pa (ref. 1 m) with and without the application of a [5,10] kHz band-pass filter. The noise contribution in the low frequencies is quite significant and presents several peaks in the [0-15] kHz frequency range.

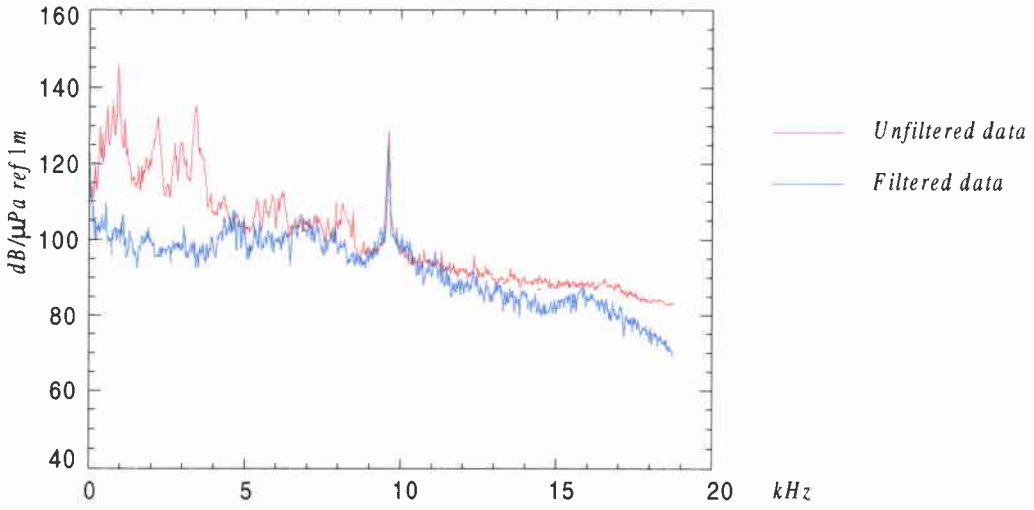


*Figure 5: Noise generated in the low frequency domain before and after analog filtering*

The ambient noise level is quite high compared to the sonar source level (210 dB/μ Pa ref. 1 m) and therefore, without any analog filtering of the data, the maximum achievable detection range could have been seriously reduced.

The power distribution indicates that most of the energy is concentrated in the 0-5 kHz range. That range is at the lower limit of the –3 dB band of the 8 kHz Ricker pulse. By filtering out the signal below *5kHz* the resulting ambient noise is reduced to 97 dB/μ Pa (ref. 1 m). Table 2 shows the power of the noise and of the emitted signal.

| | *Ambient noise* $P_n$ | *Ricker pulse* $P_s$ |
|---|---|---|
| *Unfiltered* | 120 dB/μ Pa (ref. 1 m) | 209 dB/μ Pa (ref. 1 m) |
| *Filtered* | 97 dB/μ Pa (ref. 1 m) | 205 dB/μ Pa (ref. 1 m) |

*Table 2: Noise power compared with emitted signal power (Ricker pulse)*

The noise power is defined as

$$P_n = E\{n(t)^2\} - E\{n(t)\}^2 = \sigma_n^2 \qquad P_n(dB) = -S_h + 10\log(P_n) \tag{18}$$

where $n(t)$ is the stationary random process representing the noise, measured in volt/μ Pa (ref. 1 m), and $S_h$ is the hydrophone sensitivity. The signal power $P_s$ is the mean energy measured on a time window of length $T$=0.25 ms (as used in [5] to calibrate the transmitted power).

$$P_s = \frac{1}{T}\int_T s^2(t)dt \qquad P_s(dB) = -S_h + 40\log(r) + 10\log(P_s) \tag{19}$$

$s(t)$ is the emitted signal recorded by a hydrophone placed at distance $r$ and is measured in volt/μ Pa (ref. 1 m). Figure 6 shows the minimum detectable target strength (*TS*) as a function of detection range reflecting the limitation due to the 97 dB/1μ Pa (ref. 1 m) ambient noise and a detection threshold of 10 dB without taking into account bottom backscattering. The applied transmission loss is spherical spreading which, for the low frequency range of the sonar, is a good approximation up to the range where propagation loss is no longer negligible.

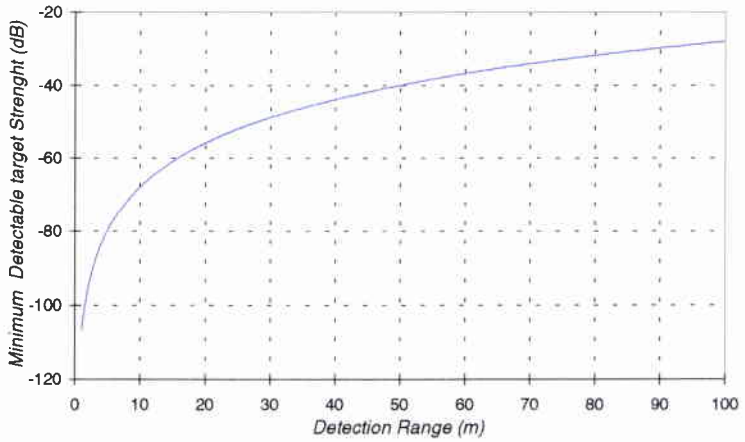


*Figure 6: Detection ranges vs. target strength*

The targets used have theoretical TS of +6 dB to –12 dB (the expected TS are around +6 dB for the cylinder and –12 dB for the sphere [7]) and should, in the noise limited case, be detectable up to at least 100 m. For buried objects placed at ~34 m (see Table 3) it is possible to have detection for a *TS* down to a maximum ~-34 dB.

### *3.3 The Target Field*

The target field was configured by GESMA and consisted initially of four targets positioned on the sea-bed, (two cylinders C1, C2 and two spheres S1, S2). Successively, two objects (a concrete block BB1, and a hollow sphere BS1) were buried in the sediment.

| *Target* | *Buried* | *Range* | *Type* | *Free field TS* | *Grazing angle* |
|---|---|---|---|---|---|
| S1 | proud | 17 m | 1 m diameter sphere (concrete filled) | -12 dB | 30.5° |
| C1 | proud | 22 m | 2 m long cylinder (end fire) | < 12 dB | 24.4° |
| BB1 | 40 cm | 34 m | concrete block | unknown | 16.4° |
| BS1 | 40 cm | 34 m | 80 cm diameter hollow sphere | -14 dB | 16.4° |
| S2 | proud | 40 m | 1 m diameter sphere (concrete filled) | -12 dB | 14.0° |
| C2 | proud | 51 m | 2 m long cylinder (broadside, LF/HF) | +3/+6 dB | 11.1° |

*Table 3: Target displacements*

A method based on sand liquefaction was used to bury the sphere (see Figure 7).

*Figure 7: sphere BS1: burial method*

### 3.4 Operations and Processing

The experiments were performed using a rail speed of 0.25 m/s, a transmitting ping interval of 0.25 s. Both Ricker pulses with a 8 kHz central frequency, and FM signals from 2 to 10 kHz with a duration of either 5 or 10 ms, were generated by the necessary high–frequency signals. Both low frequency and high frequency signals were recorded. A sonar ping was transmitted every 0.0625 m, that is less than the resulting half wavelength ($\lambda$= 0.096 m). The height from the sonar to the sea bottom was about 11 m.

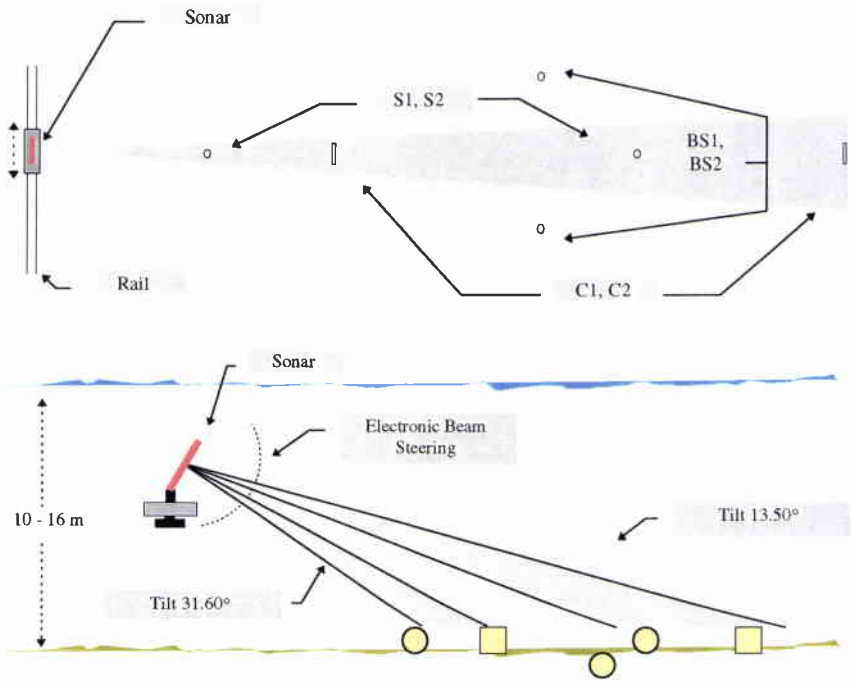


*Figure 8: Plan and section of experimental configuration*

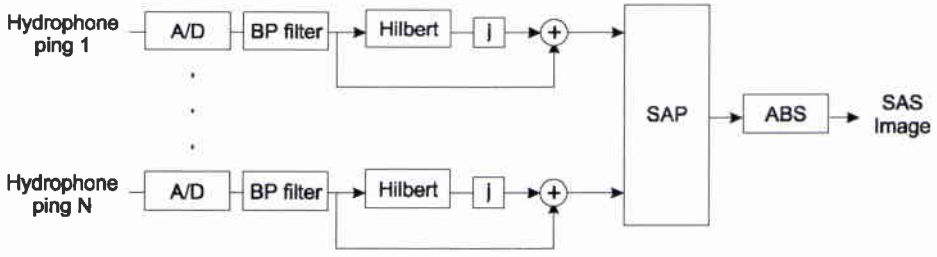


*Figure 9: SAS processing scheme*

The processing scheme is shown in Figure 9. The number of pings *N* during transit of the trolley-mounted sonar from one end of the rail to the other was about 180. Data were

sampled at a rate of 100 k sample/*s* with an accuracy of 16 bit. A band pass filter in the interval [5,10] kHz was applied to reduce the mechanical noise generated by the rail, as explained in paragraph 3.2.

# 4 Results

## 4.1 Proud targets

The first experiment was performed with partially buried objects. The two large objects present in the scene (Figure 10) are the sphere S2 (1.0 m diameter) filled with concrete, and the concrete cylinder C2 (2.0 m × 0.5 m) both partially (30-40%) covered with sand.

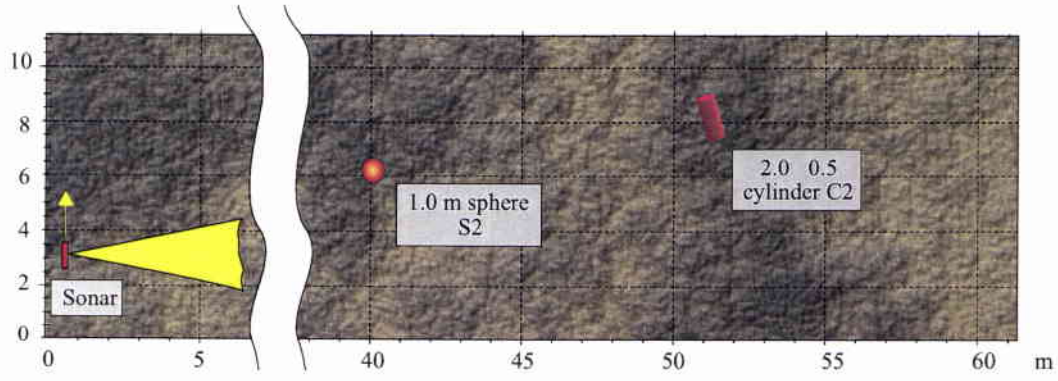


*Figure 10: SAS focused on the last two targets*

### 4.1.1 Raw data results:

Figure 11 shows the envelope of the raw data acquired during the experiment for both the primary and secondary frequencies (40 kHz and 8 kHz). The abscissa represent the traveling time $t_k$ (expressed in ms), while the ordinates are the sonar positions on the rail $x_n$ in metres.

Three targets (the sphere at ~54-55 ms and the cylinder at ~69-70 ms) and the small ring (around 67-68 ms) are clearly detected over many pings (Fig. 11). The parametric sonar receiving hydrophone has no directivity and therefore, for each target there are two echoes. The former is due to the direct path; the latter is given by the path reflected by the

sea surface. The amplitudes of the sphere echoes as a function of the sonar position $x_n$ are centered on $x_n = x_t$(sphere). The cylinder echoes have a different character as the main axes of the object were not parallel to the rail. The target strength of the cylinder has a local maximum when the sonar beam is perpendicular to the main axes of the cylinder.

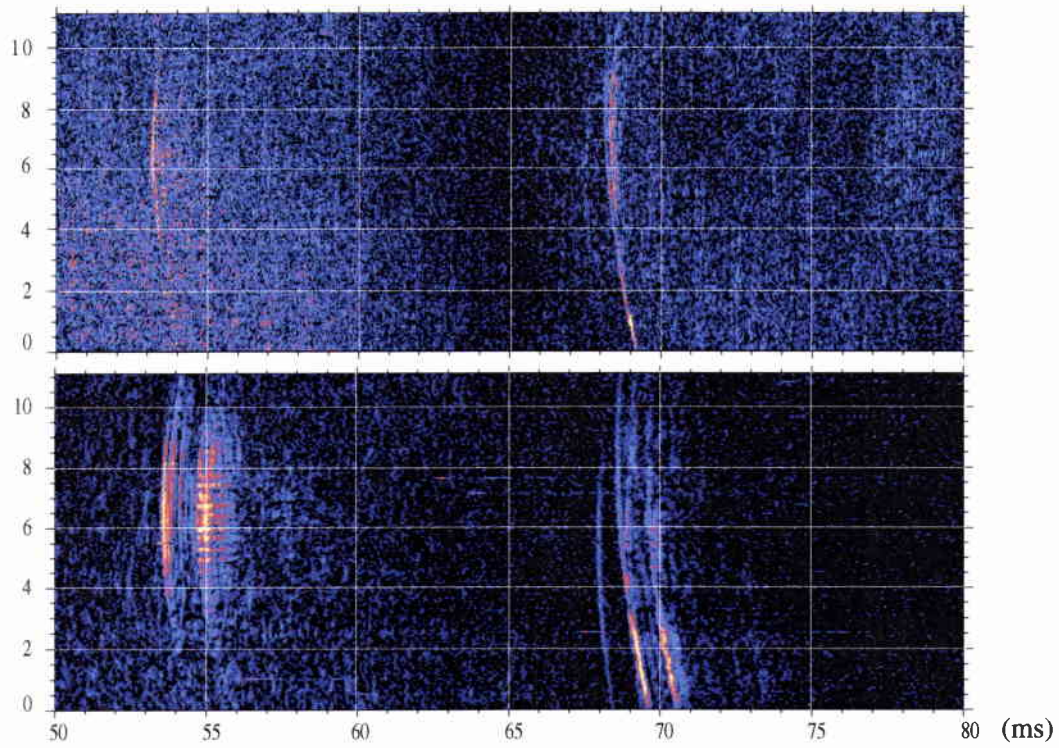


*Figure 11: Envelope of raw data (8 kHz Ricker pulse primary and secondary)*

Figure 12 and 13 present the back-scattered signals of the sphere S2 and the cylinder C2 for both the secondary and the primary frequency. For each object the raw signal (measured in volts) and the target strength (*TS*), are shown. The target strength is computed from the following formula:

$$TS = RL + TL - SL \tag{20}$$

where TL is the transmission loss (in this case only the spherical spreading $40\log_{10} r$ has been taken into account), *SL* is the sonar source level [5], and *RL* is the received power

$$RL = 10\log_{10}\frac{1}{T}\int_T v^2(t)dt \tag{21}$$

The time window length $T$ should be the same used to calibrate the sonar [5] that is 0.25 ms.

The sonar directivity is not taken into account in the computation of the *TS*. Without a precise knowledge of the geometry of the scene (exact positions and rotation of the angle dependent target like the cylinder) it is not possible obtain a correct *TS* measure. As the data for the sphere S2 were acquired with the sonar plane pointing (at the *CPA*) towards it, the maximum *TS* in Figure 12 approximates the real target strength.

The *TS* shown in Figure 13 generated by the cylinder C2 is produced by the product of the beam pattern of the sonar and the directivity of the backscattering object. Therefore without both the position and the slant of the cylinder it is impossible to evaluate the correct *TS*.

The high frequency raw signal (b) shows a greater reverberation level and a low phase coherency over many pings probably caused by the low PSRR. The expected gain of the coherent stacking performed by the synthetic aperture processing should be around 5-6 dB. Conversely, the low frequency (a) has a nearly perfect phase coherency, due to improved PSRR. A significant improvement in data quality should be expected during the synthetic aperture processing. This is also due to the LF larger beam-width.

Table 4 gives the measured target strength and the peak signal to reverberation ratio (PSRR) for the sphere. The PSRR is given by the following expression :

$$PSSR = 10\log_{10}\left(\frac{(\text{target } RL)}{E\{r_n^{\,2}\}}\right) \tag{22}$$

where $r_n$ is the reverberation signal around the target (excluding the target signal).

| *Target* | *Primary* *TS* (dB) / *PSRR* (dB) | *Secondary* *TS* (dB) / *PSRR* (dB) |
|---|---|---|
| Sphere S2 | -12 / 12 | -12 / 20 |

*Table 4: Peak Signal to Reverberation Ratios and Target Strength for sphere S2*

From this table, it can be observed that the measured Target Strength for the sphere is of the order of -12 dB, for both the primary frequency and the secondary frequency, which is completely in agreement with the theory. Furthermore, bottom backscattering levels of the order of [-25,-15] dB and [-35,-25] dB have been measured for the primary frequency and the secondary frequency.

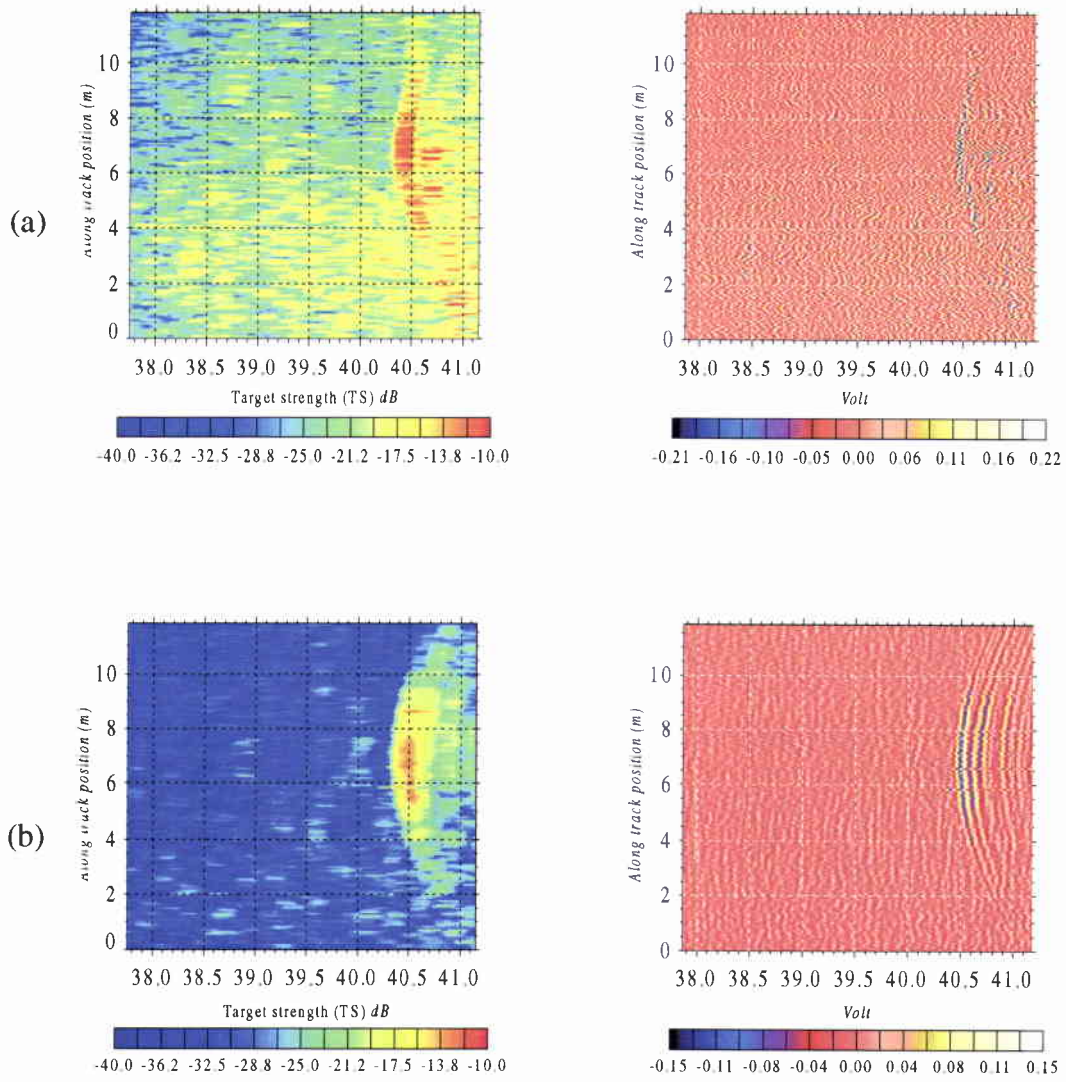


*Figure 12: Proud sphere S2, comparison between primary (a) and secondary (b) frequency for a 8 kHz Ricker pulse*

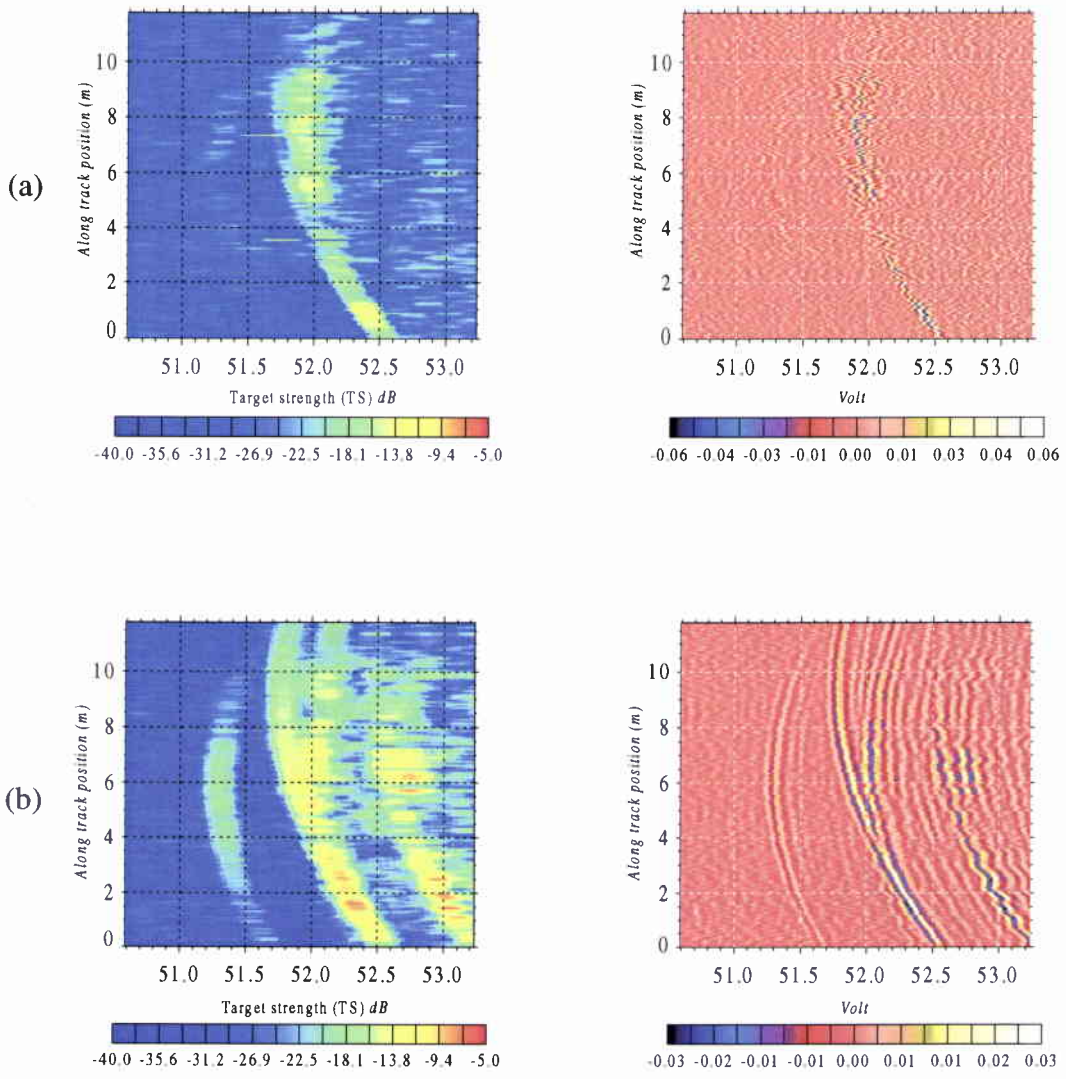


*Figure 13: Proud cylinder C2, comparison between primary (a) and secondary(b) frequency for a 8 kHz Ricker pulse*

Table 5 gives the target strength and the peak signal to reverberation ratio (*PSRR*) measured for the cylinder. It can be seen that the target strength for the cylinder is measured at -8 dB and -10 dB for the secondary frequency and the primary frequency. According to the theory it should have been of the order of +3 dB and +6 dB. However, this theoretical target strength value is the one corresponding to a cylinder seen at broadside aspect which was not the case here. The peak signal to reverberation ratio is higher, as for the sphere, for the secondary frequency component, due to the higher bottom backscattering level.

| *Target* | *Primary* *TS* (dB) / *PSRR* (dB) | *Secondary* *TS* (dB) / *PSRR* (dB) |
|---|---|---|
| Cylinder C2 | -10 / 15 | -8 / 22 |

*Table 5: Peak Signal to Reverberation Ratios and Target Strength for cylinder C2*

Regarding the peak signal to reverberation ratio, the values show a difference of the *PSRR* between the high frequency and the low one ranging from 7 to 9 dB. This is probably due to a lower reverberation level of the low frequency compared with the primary frequency.

### *4.1.2 Synthetic Aperture processing results*

Figure 14 shows the output of the virtual array for the primary frequency. The image shows the $(x,y)$ scene where $x$ is the horizontal distance from the sonar, and $y$ represents the along rail coordinate. The two images shown correspond to two different runs with grazing angles of 15° and 10° respectively. This was necessary to cover both the targets as the high frequency has a narrower beam than the secondary frequency. A minor improvement to the signal to reverberation ratio was obtained by applying the processing (see Table 6 for details). This cannot be explained by the incorrect, for this frequency range, spatial spacing between the elements of the virtual antenna that creates grating lobes. It should have been five times smaller, but the grating lobes, which occur at around 19°, are cancelled by the directivity at emission. Other factors, such as a worst medium coherency or an imprecise trigger, could have influenced the phase coherency. A significant improvement in the spatial resolution was achieved but, because of the low inter-ping phase coherency the normalized output (designated TS in Figure 14) is very weak. Both the sphere and the cylinder are placed in the correct positions and it is possible to evaluate the angle between the cylinder axes and the rail.

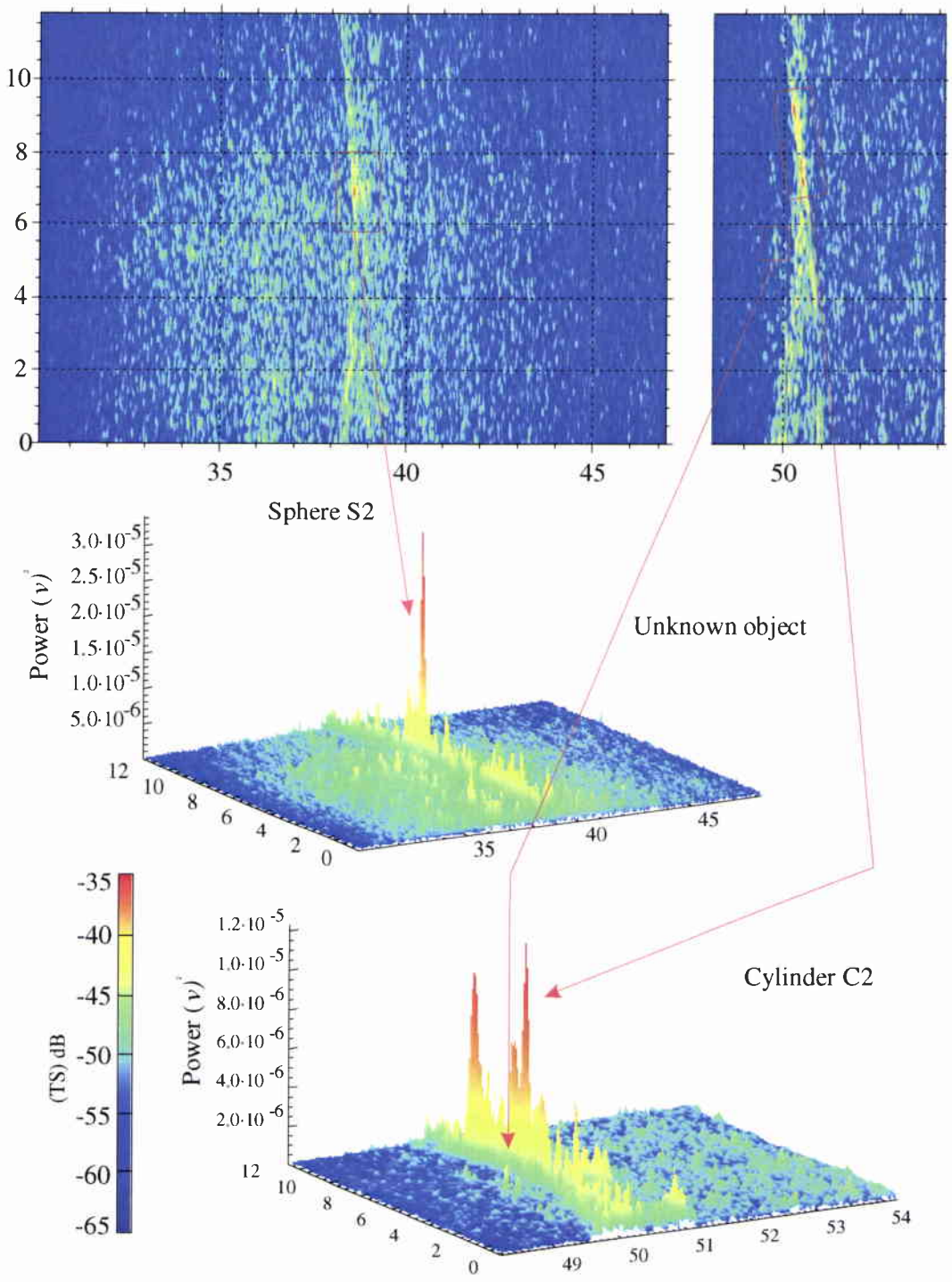


*Figure 14: Synthetic aperture image for high frequency (40 kHz)*

Figure 15 presents the output of the synthetic aperture processing for the low frequency. Again, both the sphere and the cylinder are placed in the correct positions and it is possible to evaluate the angle between the cylinder axes and the rail. A good reduction in the reverberation level has been obtained.

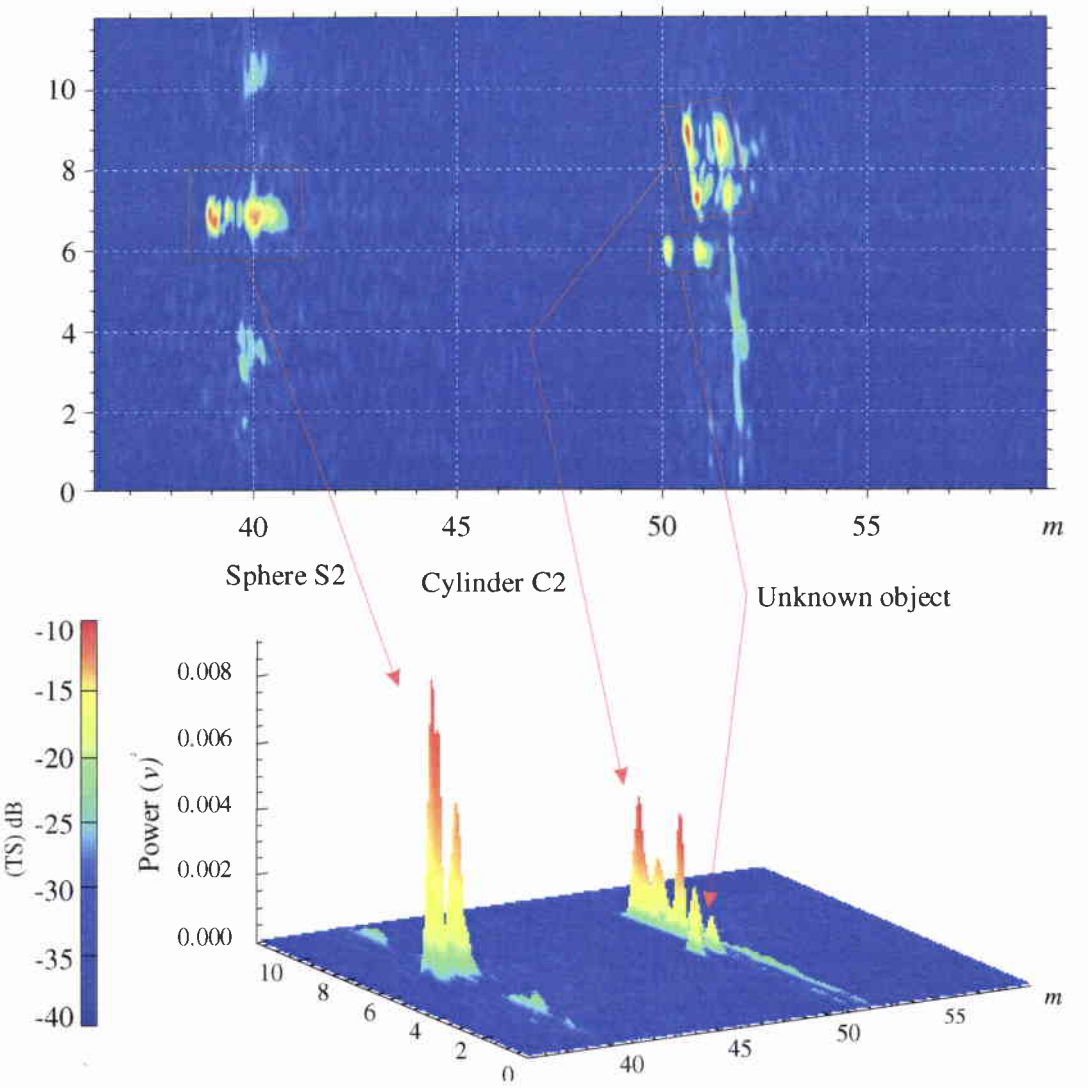


*Figure 15: Synthetic aperture image for low frequency (8 kHz)*

Table 6 presents the values of the peak signal to reverberation ratio (*PSRR*) obtained for the various targets before and after the synthetic aperture processing. The processing has increased the signal to reverberation ratio by more than 10 dB for the secondary frequency and of about 5-8 dB for the primary frequency.

| *Target* | *40 kHz Ricker PSRR* (dB) | *SAS image of 40 kHz Ricker* (dB) | *8 kHz Ricker PSRR* (dB) | *SAS image of 8 kHz Ricker* (dB) |
|---|---|---|---|---|
| Sphere S2 | 12 | 18 | 20 | 31 |
| Cylinder C2 | 15 | 20 | 22 | 30 |

*Table 6: Peak Signal to Reverberation Ratios of unprocessed and processed signals*

The side-lobes of the target in the SAS data are very low as shown in Figure 16(a)(b) and Figure 17(a)(b). These plots present the variation of the energy (in dB normalized to the maximum on the target) around the targets as a function of the along rail co-ordinate. In particular, each plot shows the behaviour of the unprocessed data (red dashed line) and the result of the SAS applied to the real target (blue solid line).

(a)

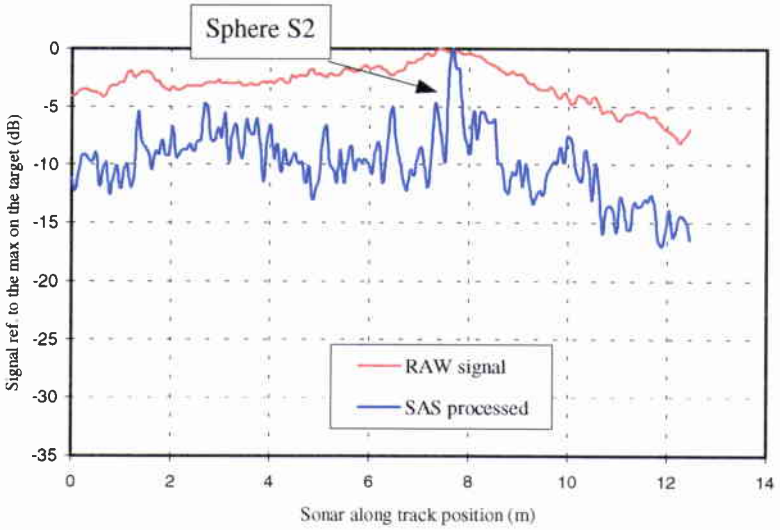


(b)

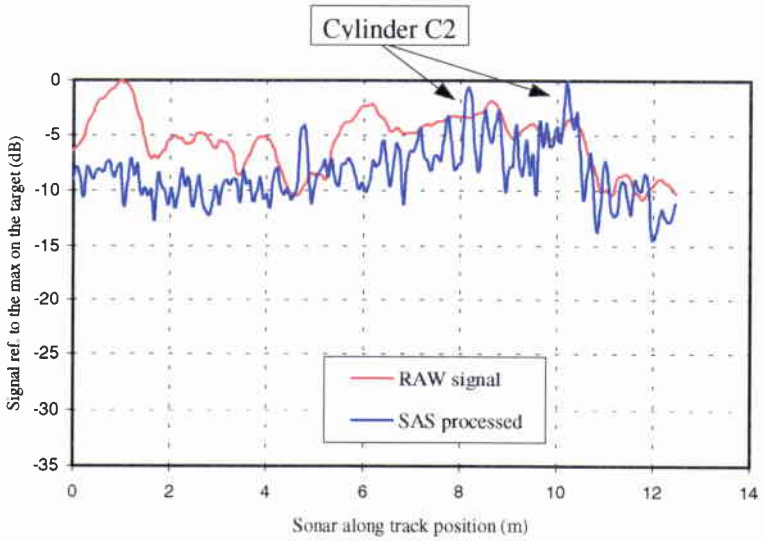


*Figure 16: Variation of signal levels for (a) sphere S2 and (b) cylinder C2 for the primary frequency (40 kHz)*

(a)

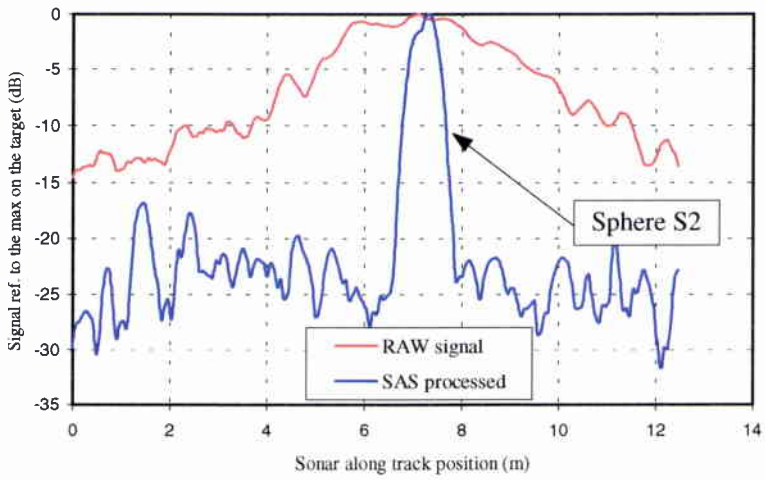


(b)

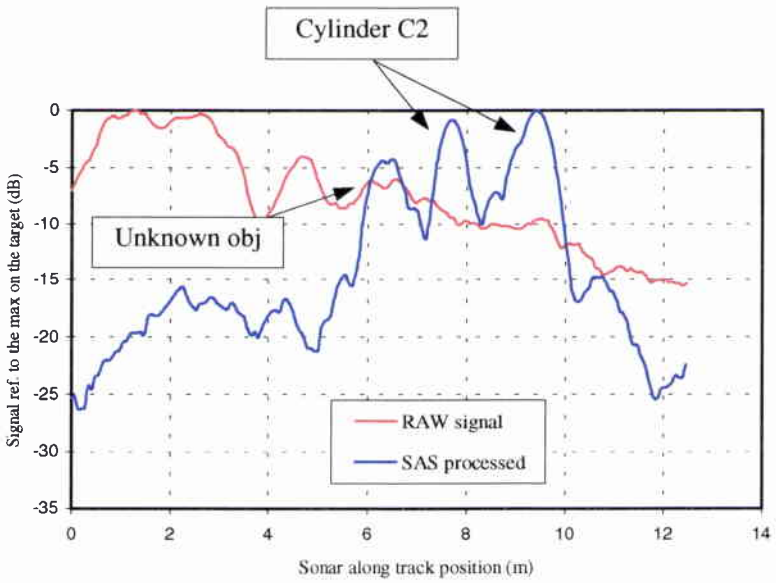


*Figure 17: Variation of signal levels for (a) sphere S2 and (b) cylinder C2 for the secondary frequency (8 kHz)*

### 4.2 Buried Targets

The second experiment was performed with a 0.80 m diameter iron sphere filled with water as shown in Figure 18 and a buried concrete block which was already there in the previous experiment. These two buried objects were at approximately the same distance from the rail.

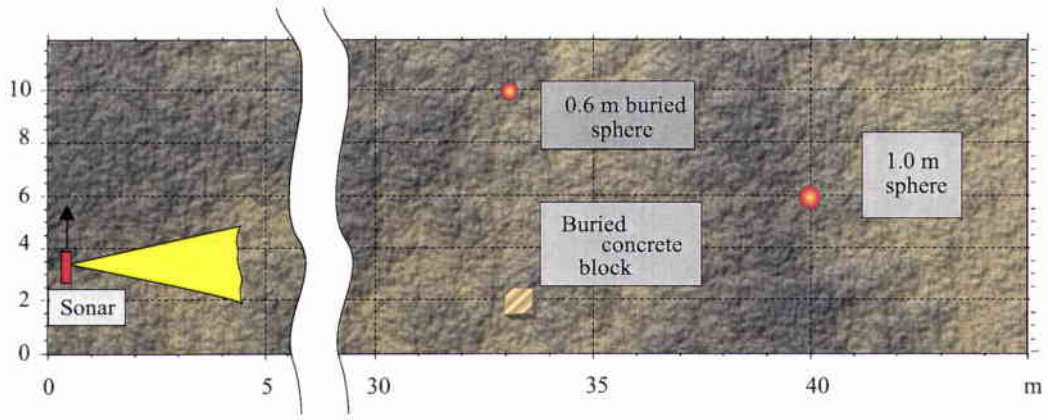


*Figure 18: Buried target positions*

#### 4.2.1 Raw data results:

Figure 19 shows the envelope of the raw data for the primary (a) and secondary frequency (b). The abscissa represent the travelling time $t_k$ expressed in ms, the ordinates the sonar positions on the rail $x_n$. Some problems were encountered during the data recording and the traces present "holes" in the low frequency signals probably caused by an intermittent connection. Due to this drawback, the signals are extremely noisy. In addition the ping rate was no longer 4 ping per second (pps) but was reduced to 2 pps and therefore the virtual antenna spacing was 0.0125 m which is half a lambda at 6 kHz.

The stronger echo in the low frequency image (from 53 to 55 ms) is the proud sphere *S2* already analyzed. The same target in the primary channel data causes a weaker echo because of the narrower beam of the high frequency sonar. In both channels there is an area with strong reverberation from 45 to 50 ms in the first 6 m of rail. This reverberation was also present in the previous data (with the proud targets) and corresponds to the position of the buried block *BB1*. On the other side of the rail, from 6 to 12 m it is possible to identify the trace (a *smile* function) generated by the buried sphere *BS1* just in the low frequency.

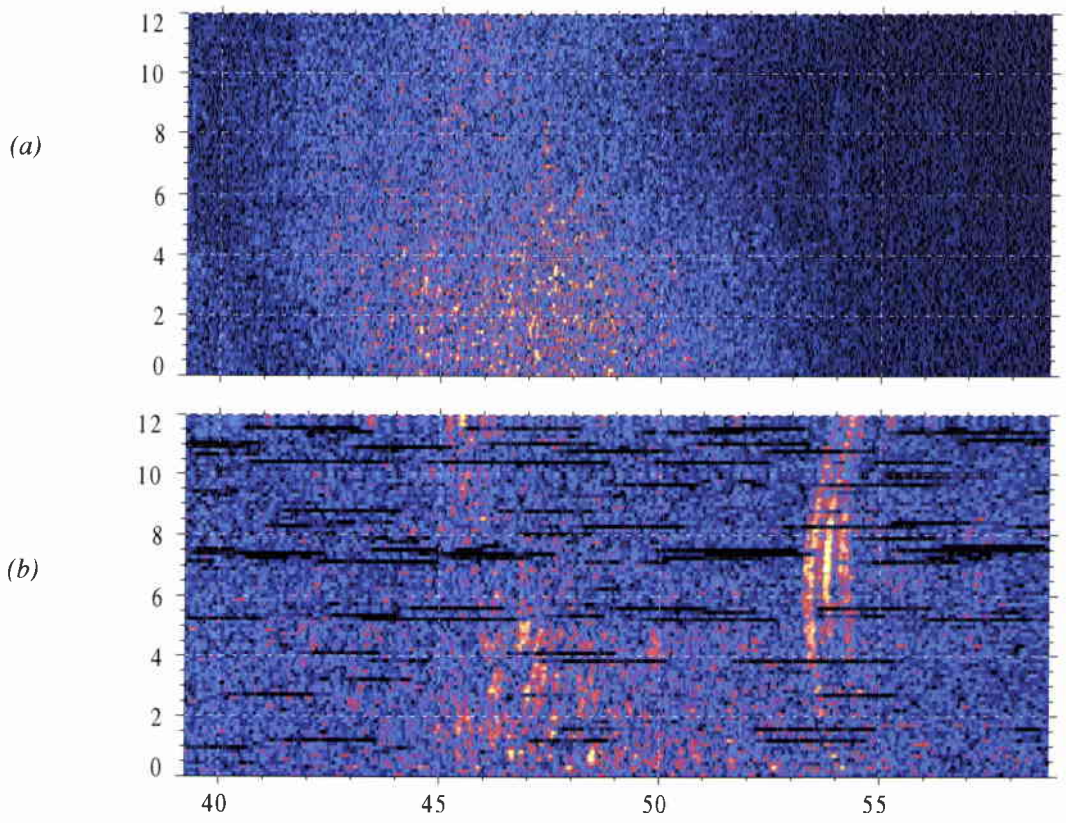


*Figure 19: Envelope of raw data for the buried objects; 8 kHz Ricker both primary (a) and secondary frequency (b)*

Figure 20 and Figure 21 present the back-scattered signal of the area in which the buried targets were expected (respectively *BS1* and *BB1*). As already presented for the proud objects, the pictures show the raw signal (measured in *volt*) and a normalized energy that give an indication of the target-strength *TS* given by Eq. (18) and Eq. (19).

Note that the buried sphere is clearly identifiable by means of the low frequency data in both the energy (*TS*) and the raw signal (in the raw signal there is a good phase coherency). A weak signal is also present in the primary frequency energy map but not in the raw signal because of the phase incoherence.

Table 7 respectively gives the target strength and the peak signal to reverberation ratio (PSRR) measured for the sphere. The numbers show a difference of only 8 dB with the free field theoretical *TS* (-14 dB) which correspond to the absorption and attenuation into the sediment. This result emphasizes that sub-critical penetration into the sediment is possible.

| *Target* | *Primary* *TS* (dB) / *PSRR* (dB) | *Secondary* *TS* (dB) / *PSRR* (dB) |
|---|---|---|
| *Buried sphere BS1* | -25 / 5 | -22 / 10 |

*Table 7: Peak Signal to Reverberation Ratios and Target Strength for buried sphere BS1*

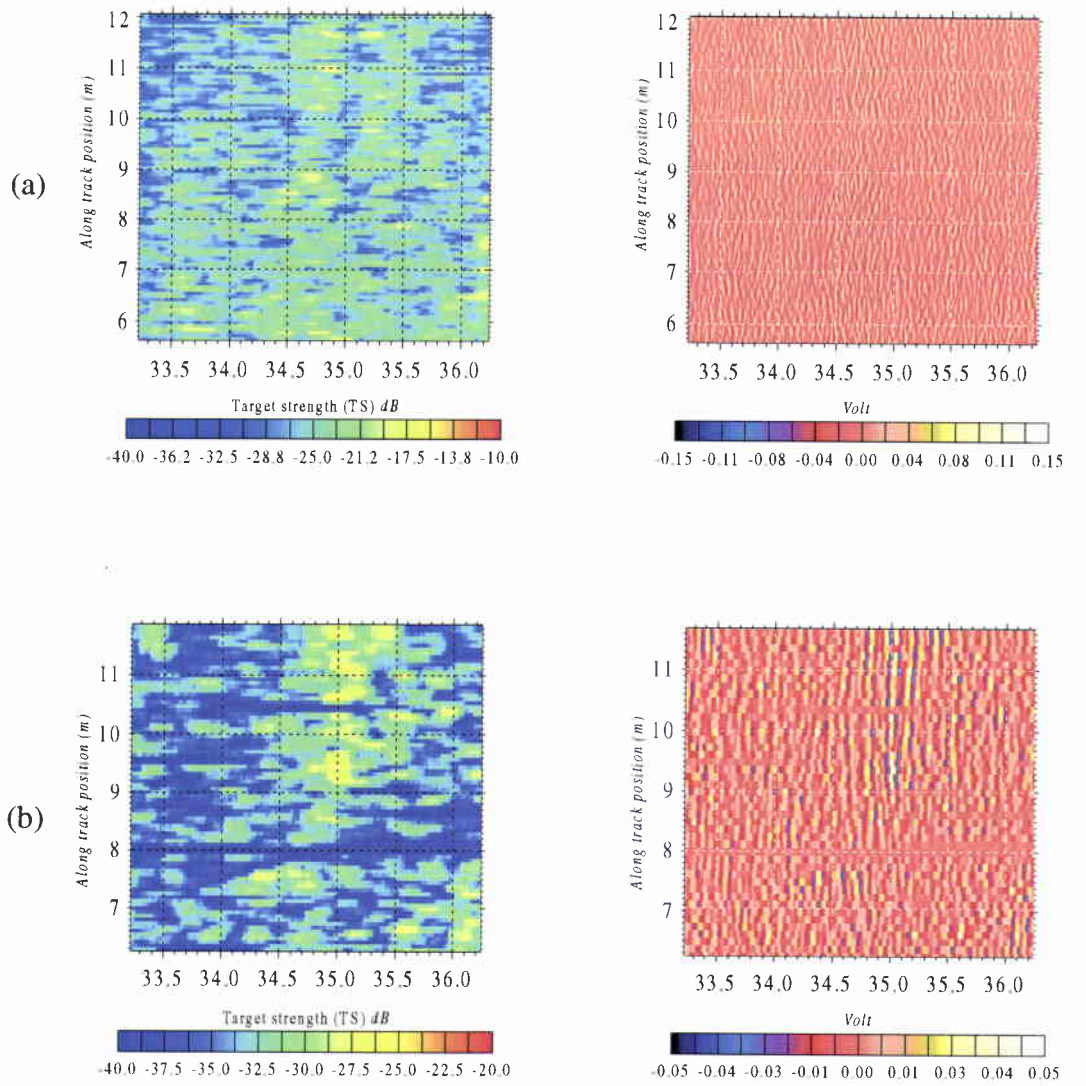


*Figure 20: Buried sphere BS1, comparison between primary (a) and secondary (b) frequency for a 8 kHz Ricker pulse*

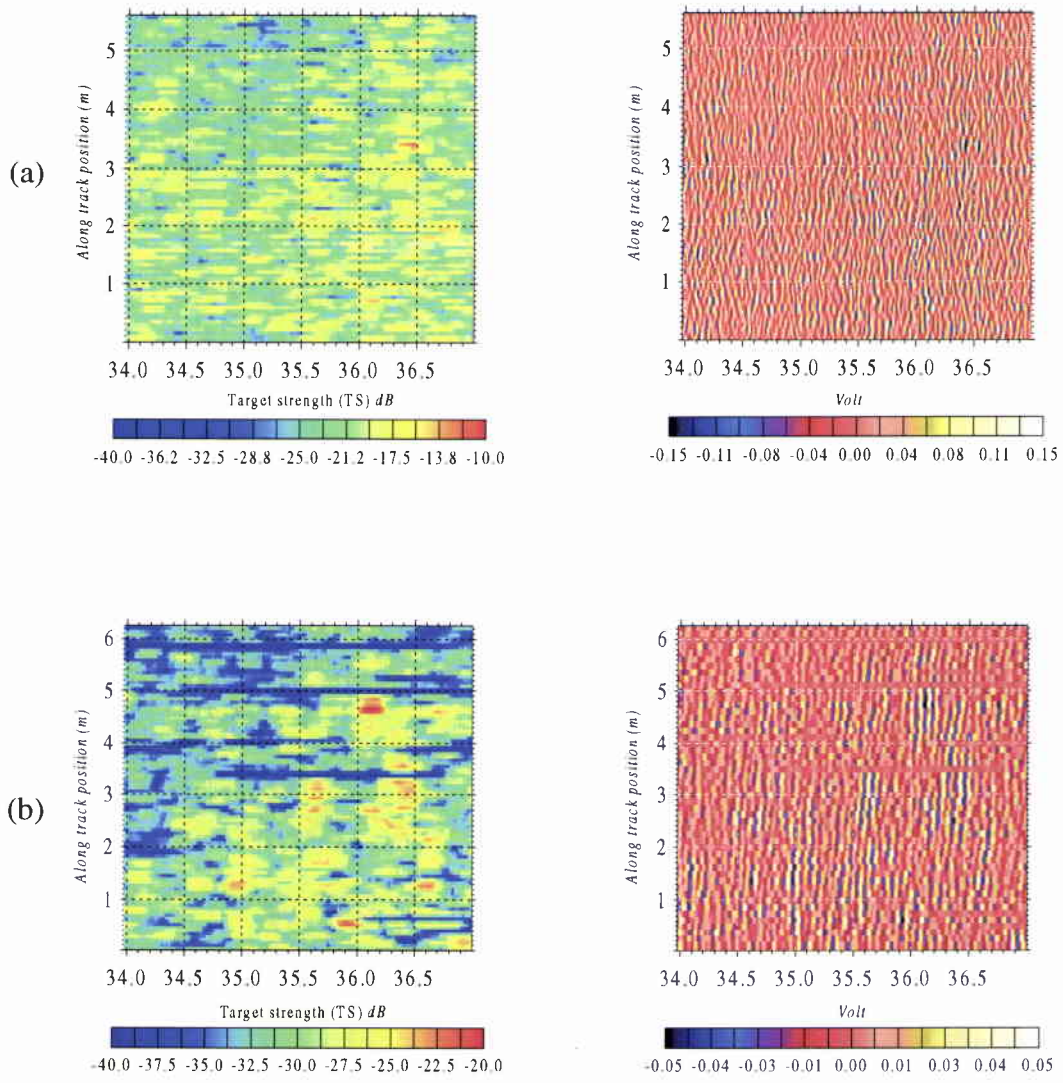


*Figure 21: Buried block BB1, comparison between primary (a) and secondary (b) frequency for a 8 kHz Ricker pulse*

The presence of many scattering point characterizes the area around the target *BB1* shown in Figure 21. It is not possible to identify a single target. Therefore the values of the target strength and *PSRR* presented in Table 8 are meaningless.

| *Target* | *Primary* *TS* (dB) / *PSRR* (dB) | *Secondary* *TS* (dB) / *PSRR* (dB) |
|---|---|---|
| *Buried block BB1* | -18 / 7 | -21 / 9 |

*Table 8: Peak Signal to Reverberation Ratios and Target Strength for buried block BB1*

### 4.2.2 Synthetic Aperture processing results

The same SAS processing was applied to the data acquired in October (therefore without the additional buried target) and in March with the new buried sphere. The transmitted pulse was, in both cases, a FM sweep from 2 to 10 kHz with a length of 5 ms and the SAS was performed after the chirp-pulse compression through a matched filter. Figure 22 shows the result on the complete target field with all the four objects on the bottom. The stronger echoes in both images are given by these proud objects: from the left to the right one can detect the sphere *S1*, the end-fire cylinder *C1*, the sphere *S2*, and the nearly-broadside cylinder *C2*. The differences in the reverberation level between *C1* and *S2* are due to a different Time Variable Gain (*TVG*) applied to the two images to compensate the transducer beam pattern..

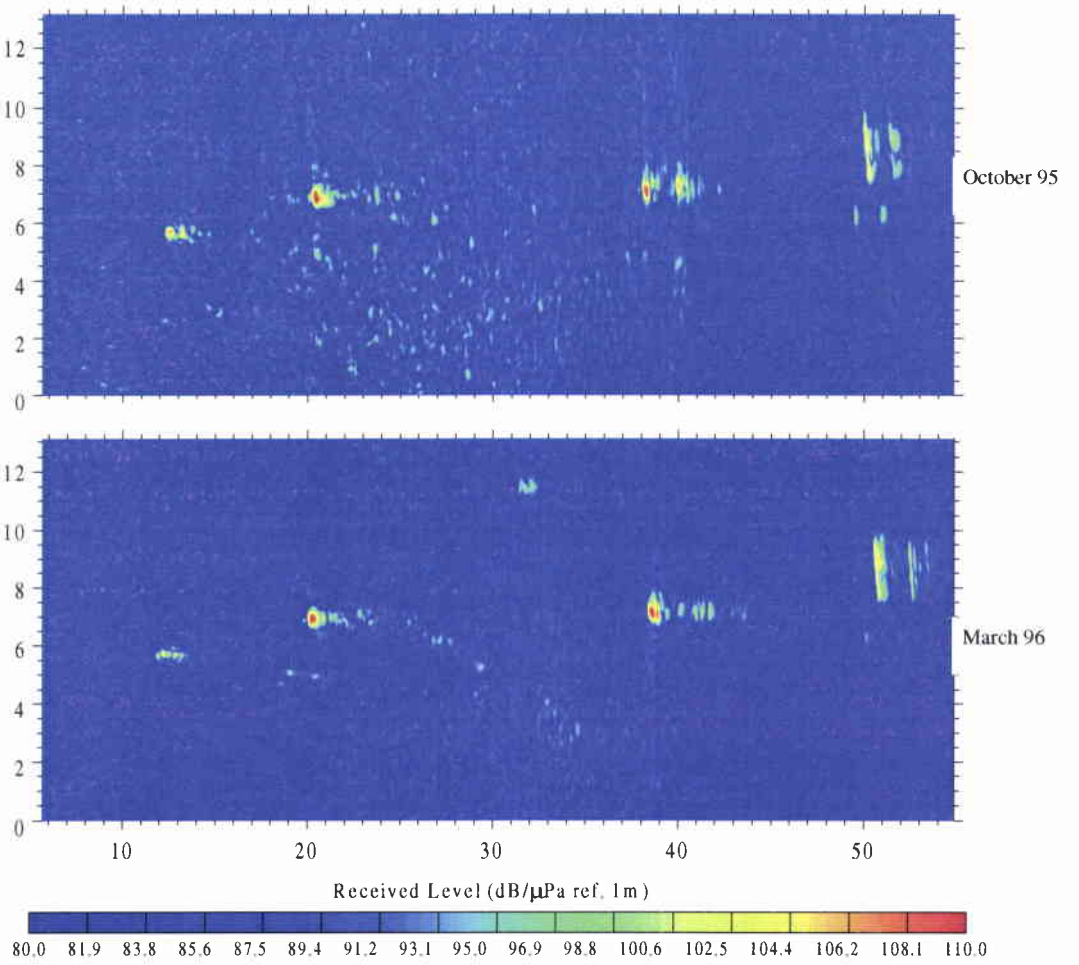


*Figure 22: Comparison between October and March SAS processed data*

There are small scattering points which share the same position in both sets of data but in the March image there is a new object between the cylinder *C1* and the sphere *S2* in the upper part which is clearly the buried sphere *BS1*.

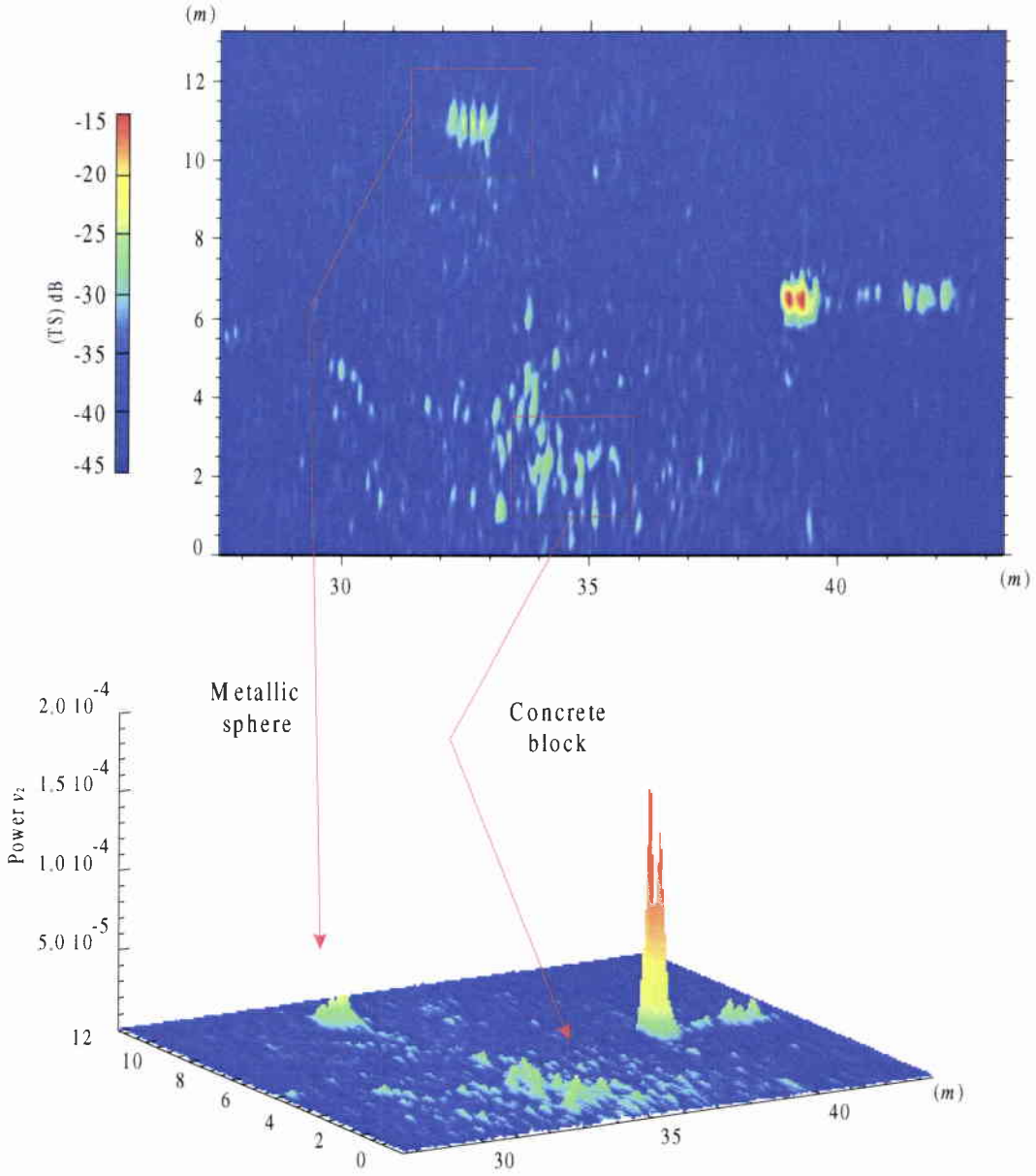


*Figure 23: Synthetic aperture image for low frequency (8 kHz)*

Figure 23 show the SAS processed data for the area around the buried objects. The transmitted pulse is in this case a 8 kHz ricker. The object *BS1* is well detected and

correctly placed. It is important to note (Figure 24) that the back-scattered echo presents a structure that differs from the proud sphere: there are four return signals instead of the two which characterize the sphere *S2*.

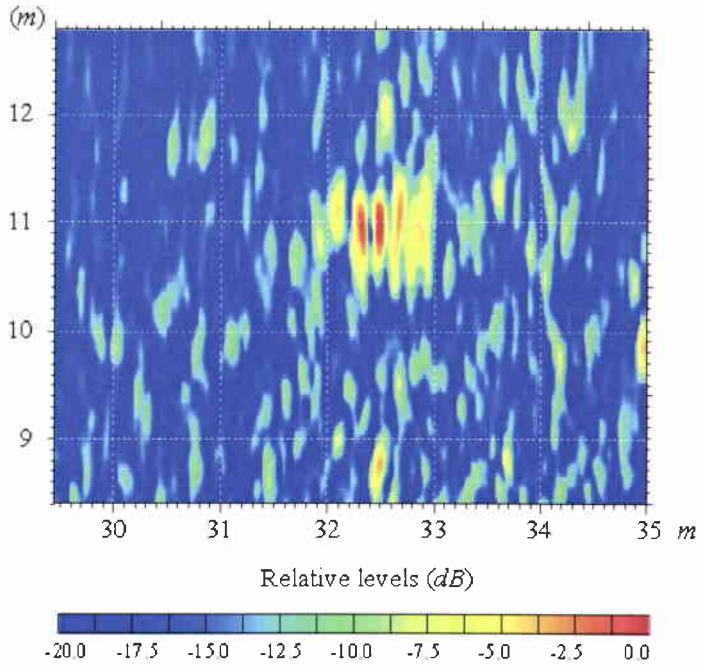


*Figure 24: SAS result for the buried sphere*

On the other side of the rail, it is possible to identify many scattering points but not a single object.

Figure 25 shows the profile of the signal levels as a function of the sonar position before and after SAS processing for the two buried objects. The presence of the buried sphere is clear from the data. That the reduction of bottom reverberation is not as significant as for the October experiment is probably due to the fact that the objects are not at the centre of the antenna field, data recorded at a lower ping rate and additional noise.

This can be confirmed by Table 9 which presents the values of *PSRR* before and after SAS processing for the two buried objects. An increment of 8 dB has been obtained for both the buried and the proud sphere. The SAS processing has revealed several scattering points where the *BB1* is expected and therefore no increment in the *PSRR* is predicted.

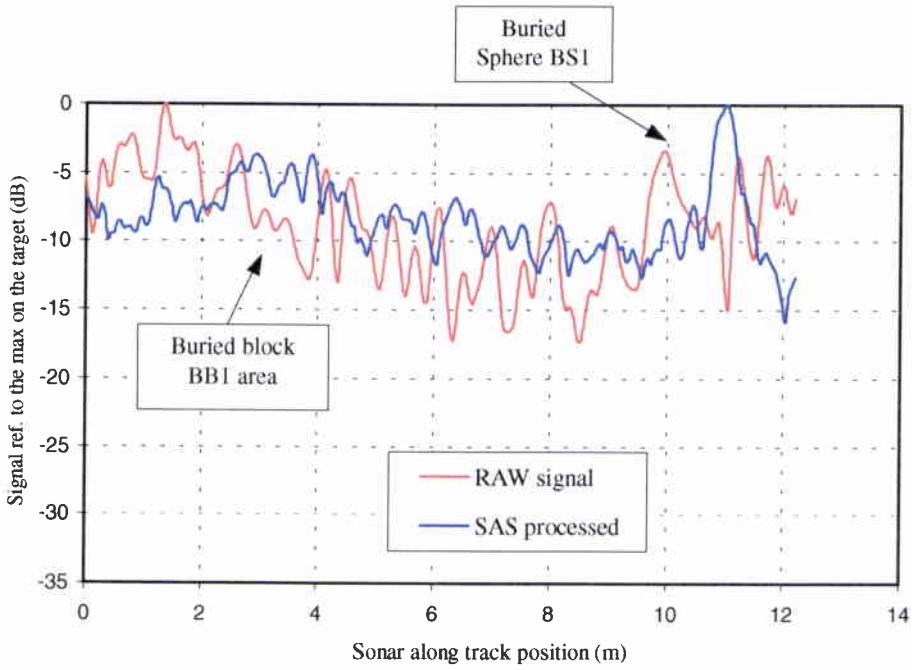


*Figure 25: Variation of signal levels as a function of the sonar position before and after SAS processing for the buried objects*

| *Target* | *8* kHz *Ricker PSRR (dB)* | *SAS image of 8* kHz *Ricker* (dB) |
|---|---|---|
| Sphere S2 | 22 | 30.0 |
| Buried Sphere BS1 | 10 | 18 |
| Buried Block BB1 | 9 | 11 |

*Table 9: Peak Signal to Reverberation Ratios of unprocessed and processed signals*

A very weak buried target could be identified in the high frequency and the expected improvement after the SAS processing will not be sufficient to separate the target from the reverberation background. Therefore there is no need to show the result of the SAS processing applied to the 40 kHz signals.

intentionally blank page

# 5 Conclusions

It has been demonstrated that the detection of buried objects is possible using sonar at grazing angles below the critical angle with only a few dB loss between the measured and theoretical TS of the buried and proud sphere respectively. Further studies and experiments will be performed in order to investigate the underlying physics of sub-critical angle penetration into the sediment and to estimate the performance of the TOPAS sonar for the detection of buried objects.

It was also demonstrated that, for the bottom type considered, the low-frequency results were better than the high-frequency results for proud targets. This result is explained by the difference of reverberation level. The high-frequency reverberation level was measured 10 dB higher than the low-frequency reverberation level.

Synthetic Aperture Processing was shown to significantly improve the performance obtained with the parametric sonar. The processing gain of Synthetic Aperture Processing was measured equal to 10 dB and 8 dB for the proud and buried targets respectively. Synthetic Aperture Processing was also shown to estimate precisely the targets position and also the targets orientation. However, it must be remembered that it was applied in ideal conditions (no platform motion). Further work will be performed in order to estimate the sensitivity of the Synthetic Aperture processing to the motion of the tow-body supporting the TOPAS sonar. It is likely that using broadband low-frequency signals would favor of the Synthetic aperture processing which should improve the spatial resolution gain. It is also the intention to start work on the auto-focusing techniques that could be applied to Synthetic Aperture Processing in order to accurately estimate the platform motion and therefore take into account in the equations used for performing the focusing of the data.

intentionally blank page

# A

# Description of the Parametric Source

The parametric sonar used was the SIMRAD TOPAS (TOpographic PArametric Sonar). Within the TOPAS the generation of a short single pulse is obtained by transmitting a weighted HF-burst at the primary frequency. The TOPAS transducer consists of 24 staves, electronically controlled to form a beam in a selected direction (~ 40°). The primary frequency is 40 kHz, the difference frequency from 1 kHz to 10 kHz. The transmitting source is of the order of 243 dB for the primary frequency. The source levels [10] obtained at different frequencies vary from about 190 to 213 dB/1 μ Pa ref. 1 m (see Table 10) using frequency from 1 to 10 kHz.

| *Pulse* | *Beam Width HP/LF (-3* dB) | *band Width LF (-3*dB) | *LF SL* (db/1 μ Pa) | *HF SL* (db/1 μ Pa) |
|---|---|---|---|---|
| Ricker 10 kHz | 2.1°/5.5° | 6 kHz | 208.6 | 241.5 |
| Ricker 8 kHz | 2.2°/5.5° | 7 kHz | 209.9 | 242.3 |
| Ricker 5 kHz | 2.2°/5.5° | 6 kHz | 212.4 | 244.9 |

*Table 10: Source level measurements*

The beam pattern of the difference frequency has good directivity (almost the same as for the high frequency conventional sonar) and extremely low side-lobes as shown in Figure 26.

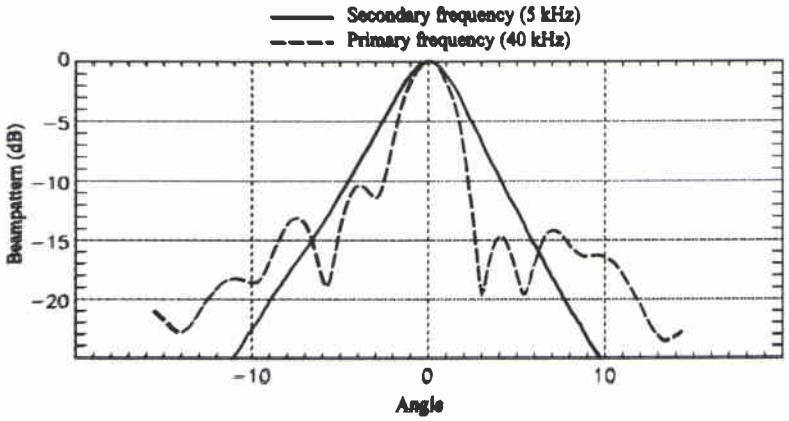


*Figure 26: Beam pattern for high and low frequency*

The receiving system of the parametric sonar consists of 3 different receiving hydrophones: for the primary frequency (40 kHz), for the difference frequency (low frequency), and for harmonic frequencies (80 kHz). Raw data can be stored directly on a workstation hard-disk at a rate of 100 k sample/*s* up to 400 k sample/*s*.

# References

[1] Pethersen, J. M. Hovens, and A. Lovik, A new sub-bottom profiling sonar using a non-linear sound source, *Radio and Electrical Engineering*. **47**, 1977:105-111,

[2] Chotiros, N. Biot model of sound propagation in water-saturated sand, *Journal of the Acoustical Society of America*, **97**, 1995:199-234.

[3] Thorsos, E.I., Jackson, D.R., Moe, J.E., Williams, K.L. Modelling of subcritical penetration into sediments due to interface roughness. In: Pace, N.G., Pouliquen, E., Lyons, A., Bergem, O., editors. High-frequency Acoustics in shallow water. Lerici, 30 June to 4 July 1997. La Spezia, Italy, NATO SACLANT Undersea Research Centre, 1997. [ISBN 88-900194-1-7].

[4] Jensen, F.B., Schmidt, H. Subcritical penetration of narow gaussian beams into sediment, SACLANTCEN SR-134. La Spezia, Italy, NATO SACLANT Undersea Research Centre, 1988

[5] Stephen, R.A. Bolmer, S.T. The direct wave root in Marine seismology, *Bulletin of the Seismological Society of America*, **75**, 1985:57-67.

[6] Williams, E. Creating an acoustic synthetic aperture in the ocean, *Journal of the Acoustical Society of America*, **60**, 1976:60-73.

[7] Urick, R.J. Principles of Underwater sound.

[8] Pusone E.,Lloyd, L. J. Synthetic-aperture sonars: performance analysis of beamforming and system design. SACLANTCEN SR-91, La Spezia, Italy, SACLANT Undersea Research Centre, 1985.

[9] Chatillon, M., Bouhier, E., Zakharia, M. E. Synthetic aperture sonar for seabed imaging: relative merits of narrow-band and wide-band approaches, *IEEE Journal of Oceanic Engineering*, **17**, 1992:80-94.

[10] Bergem, O., Pace, N. G. Calibration of the TOPAS PS040. Part 1: measurements recorded with TOPAS acquisition system, SACLANTCEN M-119, La Spezia, Italy, SACLANT Undersea Research. Centre, 1995.

## Acknowlegments

Many thanks go to the GESMA (Groupe d'Etudes Sous-marines de l'Atlantique) in Brest (FRANCE) which provided the rail test facility and all the necessary technical assistance.

**Report no. changed (Mar 2006): SR-268-UU**

# Document Data Sheet

| Security Classification | | Project No. |
|---|---|---|
| NATO UNCLASSIFIED | | 031-1 |
| **Document Serial No.** | **Date of Issue** | **Total Pages** |
| SR-268 | December 1997 | 47 pp. |


**Author(s)**

Fioravanti, S., Maguer, A., Løvik, A.


**Title**

A Parametric Synthetic Aperture Sonar for Detection of Proud and Buried Mines


**Abstract**

This paper describes an experimental comparison between a parametric sonar and a conventional sonar for the detection of small objects on and in, the sea bed. Two experiments were performed in France (GESMA site) in October 95 and March 96 in order to assess the feasibility of detecting buried mines using a parametric sonar configured as a sidescan sonar working at very low grazing angles (well below the critical angle) where the Snell theory restricts any bottom type 2 penetration of the sound into the sediment. There is however substantial evidence of penetration below the critical grazing angle which may be explained by different theories (such as for example bottom roughness, evanescent waves, Biot waves, Narrow beam-width). In the two experiments the parametric array was mounted on a platform which was able to move linearly at a constant speed (0.25 m/s) on a rail. Objects were positioned on and in the sea bed at ranges from 17 m to 60 m. The buried targets were detected at grazing angles of the order of 16:, well below the critical angle of 28:. The comparison of the Peak Signal to Bottom Reverberation Ratio (PSSR) obtained with high and low-frequency is performed for the proud and buried targets. It is shown that the PSSR is of the order of 5 dB higher for the low-frequency than for the high-frequency due mainly to the higher level of bottom reverberation at high-frequency. It is shown that detection of buried targets was only possible with low frequencies, emphasizing that sub-critical penetration into the sediment is possible. No detection was observed with the high-frequency due to the higher attenuation into the sediment at this frequency. While the sonar was moving on the rail it was possible to perform synthetic aperture sonar processing with the parametric array. Significant improvements in resolution and signal-to-noise ratio were also obtained by integrating successive pings transmitted while the sonar was in motion. The proud targets were precisely located within the mine field and gains of 10 dB and 5 dB respectively were obtained for the proud and buried targets. Keywords:



**Keywords**

Parametric sonar, Synthetic Aperture Sonar, Detection of buried objects



**Issuing Organization**

North Atlantic Treaty Organization
SACLANT Undersea Research Centre
Viale San Bartolomeo 400, 19138 La Spezia, Italy

*[From N. America: SACLANTCEN (New York) APO AE 09613]*

Tel: +39 (0)187 540 111
Fax:+39 (0)187 524 600

E-mail: library@saclantc.nato.int

**Initial Distribution for SR 268**

***Ministries of Defence***

| | |
|---|---|
| DND Canada | 10 |
| CHOD Denmark | 8 |
| DGA France | 8 |
| MOD Germany | 15 |
| HNDGS Greece | 12 |
| MARISTAT Italy | 9 |
| MOD (Navy) Netherlands | 12 |
| NDRE Norway | 10 |
| MOD Portugal | 5 |
| MDN Spain | 2 |
| TDKK and DNHO Turkey | 5 |
| MOD UK | 20 |
| ONR USA | 42 |

***NATO Commands and Agencies***

| | |
|---|---|
| NAMILCOM | 2 |
| SACLANT | 3 |
| CINCEASTLANT/ COMNAVNORTHWEST | 1 |
| CINCIBERLANT | 1 |
| CINCWESTLANT | 1 |
| COMASWSTRIKFOR | 1 |
| COMMAIREASTLANT | 1 |
| COMSTRIKFLTANT | 1 |
| COMSUBACLANT | 1 |
| SACLANTREPEUR | 1 |
| SACEUR | 2 |
| CINCNORTHWEST | 1 |
| CINCSOUTH | 1 |
| COMEDCENT | 1 |
| COMMARAIRMED | 1 |
| COMNAVSOUTH | 1 |
| COMSTRIKFORSOUTH | 1 |
| COMSUBMED | 1 |
| NC3A | 1 |
| PAT | 1 |

***Scientific Committee of National Representatives***

| | |
|---|---|
| SCNR Belgium | 1 |
| SCNR Canada | 1 |
| SCNR Denmark | 1 |
| SCNR Germany | 1 |
| SCNR Greece | 1 |
| SCNR Italy | 1 |
| SCNR Netherlands | 2 |
| SCNR Norway | 1 |
| SCNR Portugal | 1 |
| SCNR Spain | 1 |
| SCNR Turkey | 1 |
| SCNR UK | 1 |
| SCNR USA | 2 |
| French Delegate | 1 |
| SECGEN Rep. SCNR | 1 |
| NAMILCOM Rep. SCNR | 1 |

***National Liaison Officers***

| | |
|---|---|
| NLO Canada | 1 |
| NLO Denmark | 1 |
| NLO Germany | 1 |
| NLO Italy | 1 |
| NLO Netherlands | 1 |
| NLO Spain | 1 |
| NLO UK | 1 |
| NLO USA | 1 |

| | |
|---|---|
| **Sub-total** | 208 |
| SACLANTCEN | 30 |
| **Total** | 238 |